Bessel–Gauss resonator with spherical output mirror: geometrical- and wave-optics analysis

Julio C. Gutiérrez-Vega and Rodolfo Rodríguez-Masegosa

Photonics and Mathematical Optics Group, Departament of Physics, Tecnológico de Monterrey, Monterrey, Nuevo León, México 64849

Sabino Chávez-Cerda

Instituto Nacional de Astrofísica, Optica y Electrónica, Apartado Postal 51/216, Puebla, México 72000

Received May 2, 2003; accepted July 21, 2003

A detailed study of the axicon-based Bessel–Gauss resonator with concave output coupler is presented. We employ a technique to convert the Huygens–Fresnel integral self-consistency equation into a matrix equation and then find the eigenvalues and the eigenfields of the resonator at one time. A paraxial ray analysis is performed to find the self-consistency condition to have stable periodic ray trajectories after one or two round trips. The fast-Fourier-transform-based Fox and Li algorithm is applied to describe the three-dimensional intracavity field distribution. Special attention was directed to the dependence of the output transverse profiles, the losses, and the modal-frequency changes on the curvature of the output coupler and the cavity length. The propagation of the output beam is discussed. © 2003 Optical Society of America

OCIS codes: 140.3300, 140.3410, 140.4780.

1. INTRODUCTION

Interest in invariant optical fields (IOFs) was initiated in 1987 with the publication by Durnin *et al.* of the seminal paper on lowest-order Bessel beams.[1,2] Since then, Bessel, Bessel–Gauss, and newer beams have been studied frequently.[3–8] The attraction of IOFs lies in the fact that theoretically they propagate indefinitely without change of their transverse intensity distribution. Their potential applications in optical alignment, surveying, and optical interconnections make them relevant. In practice, it is possible to generate very good finite-extent approximations to IOFs, for instance in passive optical systems fed by laser light using a ring aperture and a positive lens,[1,2] refractive or diffractive axicons,[9–11] holographic methods,[12,13] or diffractive phase elements.[14]

In contrast to passive methods, several active schemes have been proposed to produce finite-aperture approximations of Bessel and Bessel–Gauss beams in resonators. Durnin and Eberly suggested some arrangements based on annular intracavity elements[15] and Uehara and Kikuchi[16] used output mirrors with annular apertures to produce conical fields, whereas Pääkkönen and Turunen[17] applied the concept of graded-phase mirrors, introduced by Bélanger and Paré,[18,19] to suggest resonators with aspheric mirrors, which conjugate the phase of the incident field to produce Bessel–Gauss modes.

Rogel-Salazar *et al.*[20,21] and Khilo *et al.*[22] proposed independently a resonator supporting Bessel–Gauss fields based on the fact that an axicon transforms an incident plane wave into a Bessel beam. The axicon-based Bessel–Gauss resonator (ABGR) has the technical advantage that it does not require intracavity optics or a special shape for the active medium, and it employs conventional mirrors (not complex-shaped mirrors) and commercially available axicons. Most of the analysis of the ABGR has centered on the description of the resonant modes for plane output mirrors. The mode profiles have been numerically studied with the classical Fox and Li algorithm, i.e., a single wave front is propagated back and forth through the cavity until it is unchanged on a round-trip propagation.[23,24] In spite of the fact that many valuable and practical results have been found with this approach, the Fox and Li method is limited, since it will yield information primarily about the dominant mode. Also, when the dominant eigenvalues are close together, convergence is intolerably slow.

In this paper we present a rigorous and detailed study of the ABGR with spherical output mirror. We employ a technique to convert the Huygens–Fresnel integral self-consistency equation into a matrix equation and then find the eigenvalues and the eigenvectors of the matrix. This method has two main advantages: It extracts the lowest N modes and their eigenvalues at one time, and its accuracy is determined by the order N of the matrix. A paraxial ray analysis is performed first to find the self-consistency condition for the stable periodic ray trajectories after one or two round trips. To do this, we propose an inhomogeneous *ABCD* ray transfer matrix for the axicon. Additionally, we use the Fox and Li algorithm in order to describe the three-dimensional intracavity field distribution of the dominant mode, to corroborate the geometrical predictions, and to confirm our results obtained with the Huygens–Fresnel integral approach.

We also study the effects of varying the curvature of the output mirror and the cavity length on the output transverse profile, the loss, and the resonance frequency shift of the lower modes. The analysis reveals that both the spherical mirror and the cavity length can be modified to minimize the losses due to diffraction and to adjust the Gaussian width of the output beam. As seen in our cal-

1084-7529/2003/112113-10$15.00

culations, the losses of the modes decrease monotonically to zero as the radius of curvature decreases, and no residual losses are seen. The propagation of the output beam is also discussed. This work consolidates and extends previous studies on Bessel–Gauss resonators.[20–22]

2. RESONATOR DESIGN AND BESSEL–GAUSS BEAMS

We briefly describe axicon transmittance and Bessel–Gauss beams in order to establish notation and to provide a reference point for necessary formulas. An axicon is an optical element with a conical refracting or reflecting surface, which transforms an incident plane wave into a converging conical wave [see Fig. 1(a)]. As depicted in Fig. 1(b), the trajectory of an input ray, excepting a ray that crosses through the center of the axicon, is always changed by a constant angle θ_0 toward the optical axis. For a thin refractive axicon with index of refraction n and wedge angle α, this angle θ_0 is given by

$$\theta_0 = \arcsin(n \sin\alpha) - \alpha \simeq (n-1)\alpha, \tag{1}$$

where the small-angle approximation $\sin\phi \simeq \phi$ has been used to simplify the expression. Assuming a time dependence $\exp(-i\omega t)$ and ignoring an irrelevant constant phase shift, the axicon is characterized by the linear radial phase factor

$$T(r) = \exp(-ik\theta_0 r), \tag{2}$$

where $k = \omega/c$ is the free-space wave number and r is the radial coordinate.

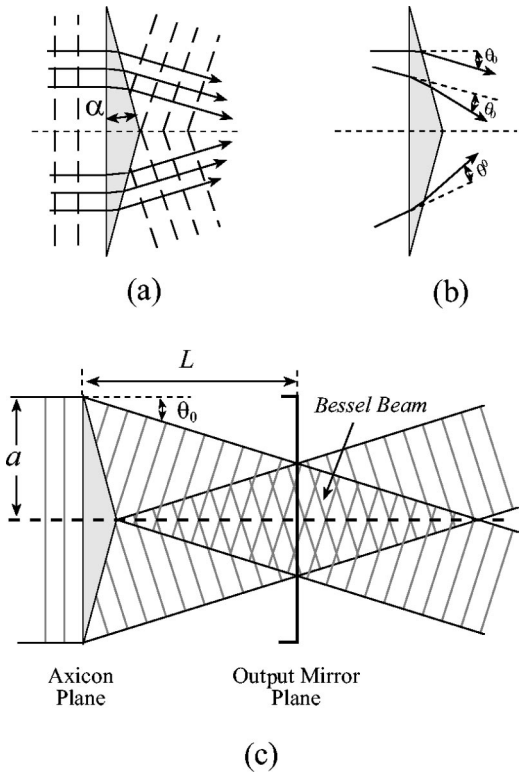

Fig. 1. (a), (b) An axicon transforms an incident plane wave into a converging conical wave. (c) The constituent plane waves of the conical waves superpose in the interference region, building up a Bessel beam.

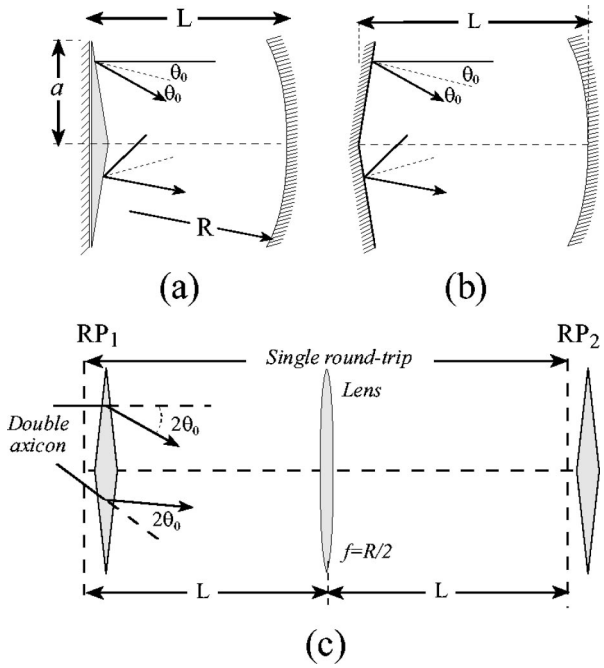

Fig. 2. Design of the resonator with (a) a refractive axicon or (b) a reflective axicon. The spherical mirror with radius of curvature R is placed a distance L from the axicon plane. (c) Lens-guide equivalent resonator. Not that light crosses twice through the refractive axicon.

As depicted in Fig. 1(c), the conical wave generated by the axicon propagates converging and emerging from the optical axis. It is known[5,11] that the field within the interference region where conical waves superpose corresponds to the Bessel beam $J_0(k_t r)\exp(ik_z z)$, where $k_t = k \sin\theta_0$ and $k_z = k \cos\theta_0$ are the radial and longitudinal spatial frequencies, respectively. If a mirror were now to be located at the output plane, the Bessel beam would be reflected upon itself. The base plane of the axicon is made to be highly reflective, whereas the output mirror is only partially reflective. In Figs. 2(a) and 2(b), we show the design of the resonator with the use of refractive and reflective axicons, respectively. The cavity length L between the axicon and the output coupler is given by

$$L = \frac{a}{2\tan\theta_0} \simeq \frac{a}{2\theta_0} = \frac{a}{2(n-1)\alpha}. \tag{3}$$

The radius of curvature R of the output coupler is a free parameter useful in changing the diffracting characteristics of the output beam. Theoretically, an ideal Bessel beam may be produced in the limit of a plane mirror ($R \to \infty$). However, referring to Fig. 2(a), within the cavity each plane-wave component of the Bessel beam will see a finite Fabry–Perot resonator. Now, it is known that the dominant mode of a parallel two-plane cavity has a bell-shaped amplitude profile,[24] therefore, even in the ABGR with plane output mirror, the resonating modes behave really as Bessel–Gauss beams.[20]

Bessel–Gauss beams with specific transverse features can be generated by choosing appropriately the geometric parameters of the resonator, including the radius of curvature of the output coupler. As we will confirm in the

following sections, because of the linearity of the paraxial wave equation, the field U at the output mirror can be considered the product of an ideal Bessel beam produced by an axicon Fabry–Perot resonator and a Gaussian beam generated by a well-known half-symmetric stable Gaussian resonator in which one mirror is planar (axicon plane) and the other is curved (output plane). The mathematical realization of this argument is

$$U(r) = J_0(k_t r)\exp(-r^2/w^2)\exp(i\Phi), \tag{4}$$

where the waist w is given by $w^2 = w_0^2[1 + (L/z_R)^2]$, with $w_0 = \sqrt{2z_R/k}$ and $z_R = \sqrt{L(R - L)}$ being the Rayleigh range of the Gaussian beam. $\Phi = kr^2/2R$ is the phase of the spherical wave front at the output mirror. The radial spatial frequency of the Bessel function is $k_t = k \sin\theta_0 = k \sin[(n - 1)\alpha]$. This means that the radial separation of the Bessel rings is dependent not on the diameter of the axicon but only on its apex angle. Equation (4) is important for practical design purposes, since it relates the characteristics of the output Bessel–Gauss beam with the resonator parameters. As is usual in two-mirror resonators, the extra phase Φ at the output coupler can be corrected easily, for instance with a converging lens.

The axicon may be considered a graded-phase mirror, and hence the ABGR falls under the category of custom laser resonators, designed to produce a prescribed intensity output profile.[18] Aspherical graded-phase mirrors have been developed to produce super-Gaussian beams[19]; however, the ABGR will generate Bessel–Gauss beams.

3. SELF-CONSISTENCY CONDITION

From a geometrical point of view, in the ABGR with plane output mirror, there is a continuous family of rays, all of them traveling with angle θ_0, which reproduce themselves after two round trips. These rays are incident on the output mirror, filling uniformly a circle of radius $a/2$ [see Fig. 1(c)]. It is expected that inclusion of the output spherical mirror instead of the plane mirror will modify the self-consistency condition for periodic stable ray trajectories within the cavity. In this section we develop a paraxial ray analysis in order to find this new condition for self-reproducing ray paths after one or two round trips.

Figure 2(c) shows the lens-guide equivalent cavity; note that a ray crosses the axicon twice in a single round-trip. The reference planes ($RP_{1,2}$) are denoted with dashed lines, and they are located just before the double axicon. The Bessel resonator is recovered in the limit $R \to \infty$. To find the stability condition, we need first the *ABCD* ray transfer matrix for the double axicon. Let (r_1, θ_1) and (r_2, θ_2) be the position and the slope of, respectively, the input and output rays crossing the double axicon. Assuming paraxiality, we have the system of inhomogeneous equations

$$r_2 = r_1,$$

$$\theta_2 = \theta_1 - 2\theta_0 = -\left(\frac{2\theta_0}{r_1}\right)r_1 + \theta_1,$$

which can be rewritten in matrix form as

$$\begin{pmatrix} r_2 \\ \theta_2 \end{pmatrix} = \begin{bmatrix} 1 & 0 \\ -2\theta_0/r_1 & 1 \end{bmatrix}\begin{pmatrix} r_1 \\ \theta_1 \end{pmatrix}. \tag{5}$$

Note that the radius r is explicitly part of the *ABCD* matrix for the double axicon, and, eventually, of the self-consistency condition. This is contrary to the typical case of two-mirror resonators supporting Gaussian beams, where the condition that rays reproduce themselves is independent of r, at least in the geometrical-optics limit. With the reference planes as shown in Fig. 2(c), the *ABCD* matrix for the complete cavity is given by

$$\begin{bmatrix} A & B \\ C & D \end{bmatrix}$$

$$= \begin{bmatrix} 1 & L \\ 0 & 1 \end{bmatrix}\begin{bmatrix} 1 & 0 \\ -2/R & 1 \end{bmatrix}\begin{bmatrix} 1 & L \\ 0 & 1 \end{bmatrix}\begin{bmatrix} 1 & 0 \\ -2\theta_0/r_1 & 1 \end{bmatrix} \tag{6a}$$

$$= \begin{bmatrix} 1 - \dfrac{2L}{R} + \left(-\dfrac{2\theta_0}{r_1}\right)2L\left(1 - \dfrac{L}{R}\right) & 2L\left(1 - \dfrac{L}{R}\right) \\ \left(-\dfrac{2\theta_0}{r_1}\right)\left(1 - \dfrac{2L}{R}\right) - \dfrac{2}{R} & 1 - \dfrac{2L}{R} \end{bmatrix} \tag{6b}$$

$$= \begin{bmatrix} D + \left(-\dfrac{2\theta_0}{r_1}\right)B & B \\ C & D \end{bmatrix}. \tag{6c}$$

Note that the *ABCD* matrix satisfies $AD - BC = 1$, since the product of matrices whose determinant is unity is also a matrix with unity determinant. We are interested in those stable trajectories inside the cavity. The mathematical problem is that of finding the eigenvalues γ and the eigenvectors (r, θ) of the self-reproducibility equation

$$\begin{bmatrix} A & B \\ C & D \end{bmatrix}\begin{pmatrix} r \\ \theta \end{pmatrix} = \gamma\begin{pmatrix} r \\ \theta \end{pmatrix}. \tag{7}$$

A 2×2 matrix has two eigenvalues (γ_a, γ_b) and two eigenvectors, which, if a constant factor is ignored, read as

$$\begin{pmatrix} r_a \\ \theta_a \end{pmatrix} = \begin{pmatrix} \gamma_a - D \\ C \end{pmatrix}, \qquad \begin{pmatrix} r_b \\ \theta_b \end{pmatrix} = \begin{pmatrix} \gamma_b - D \\ C \end{pmatrix}. \tag{8}$$

Since the matrix depends explicitly on the radius r, we need first to find the appropriate value of r in order to ensure stability. Equation (7) can be rewritten as

$$\begin{bmatrix} A - \gamma & B \\ C & D - \gamma \end{bmatrix}\begin{pmatrix} r_1 \\ \theta_1 \end{pmatrix} = 0.$$

Nonzero solutions are possible only if the determinant of the matrix vanishes; thus $\gamma^2 - (A + D)\gamma + 1 = 0$, where we have used the fact that $AD - BC = 1$. Replacing A and D from Eq. (6c) and solving for r, we obtain the eigenvalue r that satisfies self-reproducibility equation (7):

$$r = \frac{4\gamma\theta_0 L(1 - L/R)}{2\gamma(1 - 2L/R) - \gamma^2 - 1}. \tag{9}$$

Table 1. Geometrical Stability Conditions

Stability	Eigenvalue	Eigenvector	Condition
One round trip	$\gamma = 1$	$\begin{pmatrix} r \\ \theta \end{pmatrix} = \begin{pmatrix} (L-R)\theta_0 \\ \theta_0 \end{pmatrix}$	$L > R$
Two round trips	$\gamma = -1$	$\begin{pmatrix} r \\ \theta \end{pmatrix} = \begin{pmatrix} a/2 \\ \theta_0 \end{pmatrix}$	none

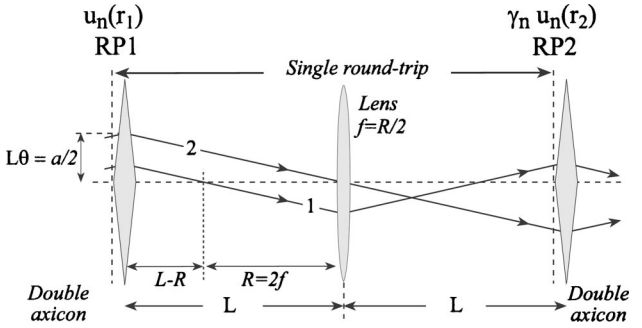

Fig. 3. Self-reproducibility condition for stable ray trajectories after one and two round trips.

To have self-reproducing trajectories after one round trip, we need $\gamma = 1$, whereas $\gamma = -1$ is required for self-reproducing after two round trips. The substitution of these special values yields

$$r_{\text{one r-t}} = (L - R)\theta_0, \qquad r_{\text{two r-t}} = L\theta_0 = \frac{a}{2}. \quad (10)$$

Once we have calculated the eigenradii and defined the eigenvalues γ, we come back to Eqs. (8) to find the eigenangles θ associated with each r. The results in both cases coincide; $\theta_{\text{one r-t}} = \theta_{\text{two r-t}} = \theta_0$. In Table 1 we summarize these results. Note that $r_{\text{two r-t}}$ is independent of the radius of curvature of the spherical mirror and, as a consequence, always is present in the cavity. On the other hand, since the radius is a quantity that is by definition positive, one-round-trip stability is possible only when $L > R$.

In Fig. 3 we show the typical two-round-trip stable trajectory. Evidently, the rays have rotational symmetry; thus we have in fact an eigencone of rays whose apex is placed at the center of the output mirror and its circular base intersects the axicon plane at radius $r = a/2$. Henceforth we will use the term "geometric cone" to refer to this characteristic cone of rays. As we will see in next sections, the geometric cone plays an important role in defining the transverse structure of the Bessel–Gauss modes. The graphical representation of the one-round-trip stability condition is also shown in Fig. 3. The eigenangle θ_0 is a restriction of the axicon, whereas the eigenradius $(L - R)\theta_0$ is determined primarily by the spherical surface.

4. WAVE-OPTICS ANALYSIS

The real behavior of the modes within the cavity is evidently affected by the wave nature of the fields and the edge-diffracted waves produced by the optical elements. We now apply the Huygens–Fresnel integral approach to find the eigenvalues and the eigenfields of the resonating modes, but fully taking into account the diffraction effects. The Huygens–Fresnel integral for the wave propagation of each azimuthal radial mode u_{lp} through a paraxial cylindrical system *ABCD*, from plane 1 [coordinates (r_1, φ)] to plane 2 [coordinates (r_2, φ)], is given by[24]

$$u_{lp}(r_2) = \int_0^\infty K_l(r_1, r_2) u_{lp}(r_1) \mathrm{d}r_1, \quad (11)$$

where $l = 0, \pm 1, \pm 2,...$ is the azimuthal mode index, $p = 1, 2, 3,...$ is the radial mode index for the mode field $u(r_1, \varphi) = \Sigma_{p=0}^{\infty} \Sigma_{l=-\infty}^{\infty} u_{lp}(r_1) \exp(il\varphi)$, and the kernel K_l is given in terms of the *ABCD* elements by

$$K_l(r_1, r_2) = (-i)^{l+1} \left(\frac{k}{B}\right) r_1 J_l\left(\frac{k}{B} r_1 r_2\right) \times \exp\left[\frac{ik}{2B}(Ar_a^2 + Dr_2^2)\right], \quad (12)$$

with J_l being the Bessel function of lth order and $k = 2\pi/\lambda$ being the wave number. An irrelevant phase factor depending on the length of the *ABCD* system has been omitted.

In Fig. 3(a) we show the lens-guide equivalent resonator. Note that we locate the RP just before the axicon and not (according to the usual practice) at the output mirror. This change allows us to consider the axicon as a plane mirror with the complex reflectivity given in Eq. (2), while the *ABCD* matrix involves only a simple air–lens–air propagation:

$$\begin{bmatrix} A & B \\ C & D \end{bmatrix} = \begin{bmatrix} 1 - 2L/R & 2L(1 - L/R) \\ -2/R & 1 - 2L/R \end{bmatrix}.$$

At the reference plane, each eigenmode u_{lp} in the cavity satisfies the self-consistency integral equation

$$\gamma_{lp} u_{lp}(r_2) = \int_0^\infty H_l(r_1, r_2) u_{lp}(r_1) \mathrm{d}r_1, \quad (13)$$

where γ_{lp} is the complex eigenvalue, given by

$$\gamma_{lp} = |\gamma_{lp}| \exp(i\beta_{lp}), \quad (14)$$

and $H_l(r_1, r_2) = K_l(r_1, r_2) T(r_1)$, with $T(r_1) = \exp(-i2k\theta_0 r_1)$ being the transmittance for the double axicon. The right-side hand of Eq. (13) is the propagation integral in the Huygens–Fresnel approximation for a complete round trip through the resonator starting at the reference plane. The operator H is neither Hermitian nor degenerate; however, it is polar. This means that instead of exhibiting power orthogonality, the eigenfunctions satisfy the biorthogonality of waves traveling in opposite directions, as demonstrated by Siegman.[24]

There are two general methods of solving Eq. (13).[25] The first one is based on iterative techniques that extract the dominant or several of the lowest-loss modes; the classical Fox and Li algorithm falls in this category. For stable resonators the iterative method usually converges slowly because even higher-order mode losses are quite low. The second method is to employ a technique to con-

vert Eq. (13) into a matrix equation by using an appropriate quadrature rule (Gaussian quadrature is usually the best choice) and then to find the eigenvalues and the eigenvectors of the matrix. The matrix method has two main advantages: It extracts the lowest N modes and their eigenvalues at one time, and its accuracy is determined by the order N of the matrix.[25,26]

Typically, the value of the radial coordinate is bounded by a maximum value where the input and output fields are small enough to be neglected; otherwise, it is bounded by the radius of the axicon. We denote as a this maximum value. Let $\mathbf{r}_1 = \mathbf{r}_2 = \mathbf{r} = [r_1, r_2, \ldots, r_N]$ and $\mathbf{w} = [w_1, w_2, \ldots, w_N]$ be the abscissas and the weight factors for Gauss–Legendre quadrature in the range $(0, a)$. If $\mathbf{u}_{lp} = [u_1, u_2, \ldots, u_N]$ is a column vector representing the eigenfield evaluated at radius $\mathbf{r}$, then Eq. (13) takes the matrix form

$$\gamma \mathbf{u}_{lp} = (\mathbf{H} * \mathbf{W}) * \mathbf{u}_{lp}, \tag{15}$$

where $\mathbf{H}$ is an $N \times N$ matrix with elements $H_{m,n} = H(r_m, r_n)$ and $\mathbf{W}$ is a diagonal matrix with elements $[w_1, w_2, \ldots, w_N]$.

The complex eigenvectors $\mathbf{u}_{lp}$ of the matrix $\mathbf{H} * \mathbf{W}$ correspond to the resonator mode patterns at the reference plane. The fractional power loss per transit of the mode due to diffraction effects at the mirrors is given by $\Gamma_{lp} = 1 - |\gamma_{lp}|^2$. As is usual in optical resonators, the eigenvalues can be sorted in decreasing magnitude order $|\gamma_1| \geqslant |\gamma_2| \geqslant \cdots$.

The phase shift β_{lp} is given by the angle of γ_{lp}, which is the phase shift suffered (or enjoyed) by the wave field in transit from one mirror to the other, in addition to the longitudinal phase shift that is given by kL. The resonant condition requires that the total phase shift Φ along the axis of the cavity be an entire multiple of π rad; thus $\Phi = kL + \beta_n = q\pi$, where q is the number of half-wavelengths of the axial standing-wave pattern. Replacing $k = 2\pi\nu/c$ and solving for the resonant frequency gives

$$\nu_{lp} = \nu_0 \left(q + \frac{\beta_{lp}}{\pi} \right), \tag{16}$$

where $\nu_0 = c/2L$ is the fundamental beat frequency, i.e., the frequency spacing between successive longitudinal resonances.

A. Resonating Modes

For numerical purposes we choose typical data from gas-discharge, fast-axial-flow cw-CO_2 laser resonators: mirror radii $a = 3/8$ in. $\simeq 10$ mm, index of refraction $n = 2.4$, axicon angle $\alpha = 0.5°$, and wavelength $\lambda = 10.6\ \mu$m. The index of refraction n and the radius a correspond to commercially available zinc selenide (ZnSe) axicons. From Eqs. (1) and (3), the cavity length is $L = 40.92$ cm and the propagation angle is $\theta_0 = 12.22 \times 10^{-3}$ rad. We use an $N = 200$ point Gauss–Legendre quadrature scheme in the range $(0,a)$ to solve the matrix equation (15).

Let us consider first the case when the output mirror is flat. The fundamental mode corresponds to the first eigenvalue for $l = 0$; theoretically, the field at the output coupler is a J_0 Bessel beam. The solution of Eq. (15) yields the eigenvalue $\gamma_{01} = 0.99106 \exp(-i0.14682)$ and the fractional power loss $\Gamma_{01} = 0.01782$.

The magnitude and the phase of the field at the reference plane u_{RP} (just before the axicon) are shown in Figs. 4(a) and 4(b), respectively. As expected, the phase curve corresponds almost exactly to the linear equation $\Theta(r) = -k\theta_0 r$; this fact confirms that the field at the axicon behaves as a conical wave.

To obtain the field u_{OM} at the output mirror, the eigenfield at the reference plane is first propagated through the double axicon and later propagated in air for a distance L until the output mirror. This propagation is performed again through the Huygens–Fresnel integral $u_{\mathrm{OM}}(r_2) = \int_0^a T(r_1) K(r_1, r_2) u_{\mathrm{RP}}(r_1) \mathrm{d}r_1$, where the kernel is given by Eq. (12), but now the *ABCD* matrix is $[1, L; 0, 1]$.

The transverse field distribution at the output mirror is shown in Figs. 4(c) and 4(d). The two curves in Fig. 4(c) correspond to the mode field calculated with the matrix approach and to the field given by the theoretical zero-order Bessel beam $J_0(k_t r)$. As discussed in Section 2, the theoretical Bessel beams produced by the resonator with plane output mirror are in fact modulated by a bell-shaped function.

We now replace the plane output mirror by a concave spherical mirror with radius of curvature $R = 10L$. The field at the axicon plane is depicted in Figs. 5(a) and 5(b). We recall from Table 1 that the ray-optics prediction for this resonator geometry corresponds to a ray emerging from the plane of the axicon at $r = a/2$ with an angle θ_0 with respect to the optical axis [see Fig. 3(a)]. This fact is in accordance with the maximum field at $r \sim a/2$ in Fig. 5(a). In Fig. 5(b) we see that the phase of the field at the reference plane is again given by $\Theta(r) = -k\theta_0 r$. Comparing Fig. 4(b) with Fig. 5(b), we note that the curvature of the output mirror introduces a negative phase shift. As we will see in Section 4, this shift is related to the Gouy phase shift induced by the spherical mirror. The output field of the ABGR with spherical mirror is shown

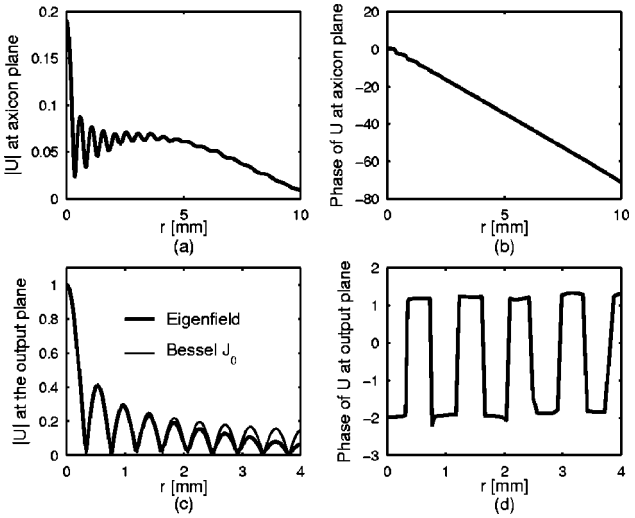

Fig. 4. Profiles of the magnitude and the phase of the eigenfield at (a), (b) the axicon plane and (c), (d) the output plane for an output flat mirror ($R \to \infty$). The thin curve in (c) represents the theoretical output Bessel beam $J_0(k_t r)$.

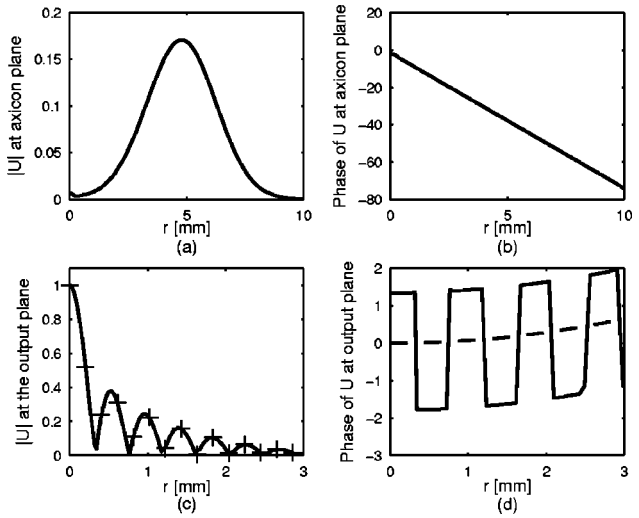

Fig. 5. Profiles of the magnitude and the phase of the eigenfield at (a), (b) the axicon plane and (c), (d) the output plane for an output spherical mirror ($R = 10L$). The plus signs represent the theoretical zero-order Bessel–Gauss beam $J_0(k_t r)\exp(-r^2/w^2)$.

Table 2. Diffractive Losses for the First Ten Modes

$R \to \infty$		$R = 10L$	
Mode (l, p)	Loss	Mode (l, p)	Loss $(\times 10^{-3})$
(0,1)	0.0178	(0,1)	0.00188
(1,1)	0.0302	(1,1)	0.00577
(2,1)	0.0593	(2,1)	0.02962
(0,2)	0.0633	(3,1)	0.04022
(1,2)	0.1072	(4,1)	0.05220
(3,1)	0.1132	(0,2)	0.06946
(0,3)	0.1583	(5,1)	0.07910
(2,2)	0.1720	(1,2)	0.10274
(4,1)	0.1984	(6,1)	0.14671
(1,3)	0.2216	(7,1)	0.34002

in Figs. 5(c) and 5(d). The field has a Bessel shape, but now the Gaussian modulation is more evident. For this particular case the intensity practically vanishes at $r = a/4 \simeq 2.5$ mm. The plus signs represent the theoretical zero-order Bessel–Gauss beam $J_0(k_t r)\exp(-r^2/w^2)$, where the width w is given by Eq. (4). The numerical and analytical approaches have yielded results that are in excellent agreement with each other. The phase of the Bessel–Gauss beam is depicted in Fig. 5(d), where the dashed curve corresponds to the spherical phase front Φ introduced by the output mirror [Eq. (4)].

Higher-order Bessel–Gauss beams are resonating modes of the cavity as well. The transverse Bessel part of these fields in Eq. (4) is given by $J_l(k_t r)\exp(il\varphi)$, where l is the integral order. The eigenmodes and the eigenvalues are calculated with Eq. (15), taking the appropriate order l in the kernel [Eq. (12)]. In Table 2 we include a list of the first ten modes sorted in ascending order by loss for plane and concave output couplers. Note that Bessel–Gauss modes produced with plane output mirrors present larger diffraction losses because they have larger mode volumes than those produced with spherical mirrors. As expected, higher-order modes have larger losses than the dominant J_0 mode, and this fact is independent of the radius of curvature. The numerical values in Table 2 confirm that the ABGR with spherical mirror offers a better modal discrimination.

Figure 6 shows the magnitude and the phase of the eigenfield corresponding to the second order $(l, p) = 21$ for a radius of curvature $R = 10L$. One can see that the general aspect of the calculated eigenfield is in quite close agreement with the theoretical second-order Bessel–Gauss beam (plus signs).

B. Effect of Varying the Radius of Curvature

Let us consider next the effect of varying the radius of curvature of the output mirror. Consider first the loss behavior corresponding to the lower-order modes resonating within the cavity. The loss Γ as a function of the normalized radius R/L is depicted in Fig. 7(a) for the first four orders $l = 0,\ldots,3$; these results were determined by finding the eigenvalues from Eq. (15) for a number of radii of curvature. Dashed lines correspond to the limiting cases when the output mirror is plane. Note that losses increase asymptotically as the radius of curvature increases.

The resonant frequency of a particular mode in the ABGR will vary if R changes. We define the relative phase shift $\Delta\beta = \beta(R) - \beta_\infty$, where $\beta(R)$ is the phase of the eigenvalue as a function of R and β_∞ corresponds to the limiting case when $R \to \infty$. The resonant frequency can be written as $\nu = \nu_\infty + \Delta\nu$, with ν_∞ being the reference frequency of the resonator with plane output mirror and $\Delta\nu$ being the frequency shift introduced when a finite radius of curvature is considered. From Eq. (16) we find that

$$\Delta\nu = \nu_0(\Delta\beta/\pi). \tag{17}$$

The normalized relative phase shift $\Delta\beta/\pi$ is depicted in Fig. 7(b) for the first four orders $l = 0,\ldots,3$. The highest curve is for the fundamental mode J_0, whereas the lowest

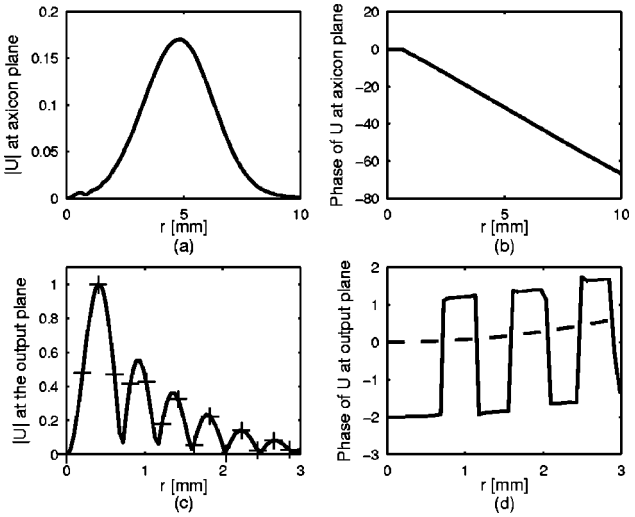

Fig. 6. Same as Fig. 5, except that the plus signs represent the theoretical second-order Bessel–Gauss beam $J_2(k_t r)\exp(-r^2/w^2)$.

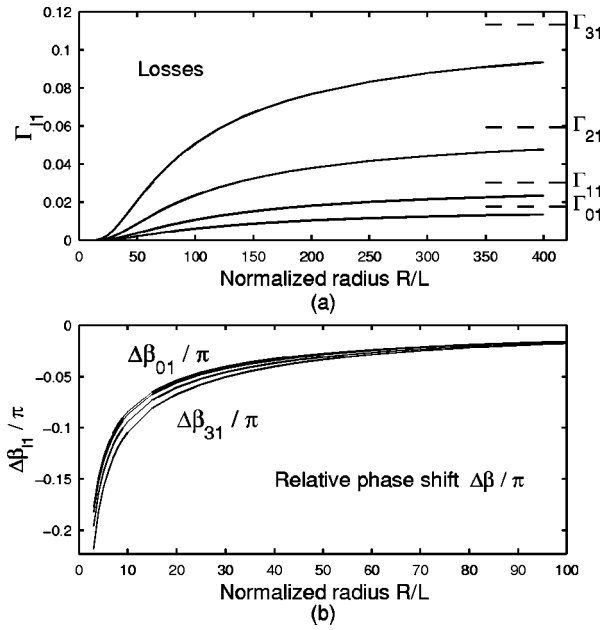

Fig. 7. Loss (Γ) and relative phase shift ($\Delta\beta/\pi$) behavior as a function of the normalized radius of curvature R/L for the first lower orders $l = 0,...,3$. The dashed lines in (a) represent the losses in the limit when R tends to infinity.

curve is for the third-order mode J_3. It is readily evident from these curves that the resonant frequency decreases as the radius of curvature of the output mirror decreases.

C. Three-Dimensional Intracavity Field Distributions

The classical Fox and Li iteration method was implemented to determine numerically the passive three-dimensional field structure of the cavity modes. For this purpose the diffractive field calculations are based on the angular spectrum of plane waves representation utilizing the fast Fourier transform algorithm. The transverse field is sampled in the reference plane over a grid of 512 $\times$ 512 points. Typically, approximately 100 round trips are required for the process to converge, starting from an arbitrary field distribution. The three-dimensional intracavity field distribution was obtained by calculating the field at 100 transverse planes evenly spaced through the unfolded cavity. Matlab software is used to implement the codes, mainly because of the existence of a wealth of built-in mathematical functions, the compact notation, and the easy way in which simulation scripts can be modified.

The intracavity field structures of the dominant and second-order modes in the ABGR with spherical mirror ($R = 10L$) are presented in Fig. 8. The axicon (at plane $z = 0$) and the output mirror (at plane $z/L = 1$) extend in transverse dimension from -1 to 1 in normalized units r/a. The pattern for the zero-order mode is rotationally symmetric, but higher-order modes have an azimuthal phase factor $\exp(il\varphi)$ and a zero field on the optical axis. The corresponding transverse fields at the axicon and output mirror planes were already calculated through the eigenequation (15) and depicted in Figs. 5 and 6.

The results shown in Fig. 8 are interesting because they clearly illustrate the strong link between the intracavity mode structure and the geometrical prediction depicted in Fig. 3 for the self-consistency condition after two round trips. Within the cavity the three-dimensional intensity distribution tends to "locate" around the wall of a geometric cone whose apex is placed at the center of the output mirror and whose circular base (radius $a/2$) is placed at the axicon plane.

We have performed a number of simulations for a variety of initial conditions, including uniform plane waves, Gaussian profiles with different widths, and random noisy transverse patterns. Regardless of the initial condition, the field always converged to the dominant mode of the cavity with the expected profile and radial frequency characteristics imposed by the geometry parameters. To induce the second-order field distribution shown in Fig. 8(b), we used initial conditions of the form $f(r)\exp(i2\varphi)$.

5. EFFECT OF CHANGING THE CAVITY LENGTH

The relationship between the axicon parameters and the cavity length given by Eq. (3) seems to be very restrictive; thus, from a practical point of view, it is of great interest

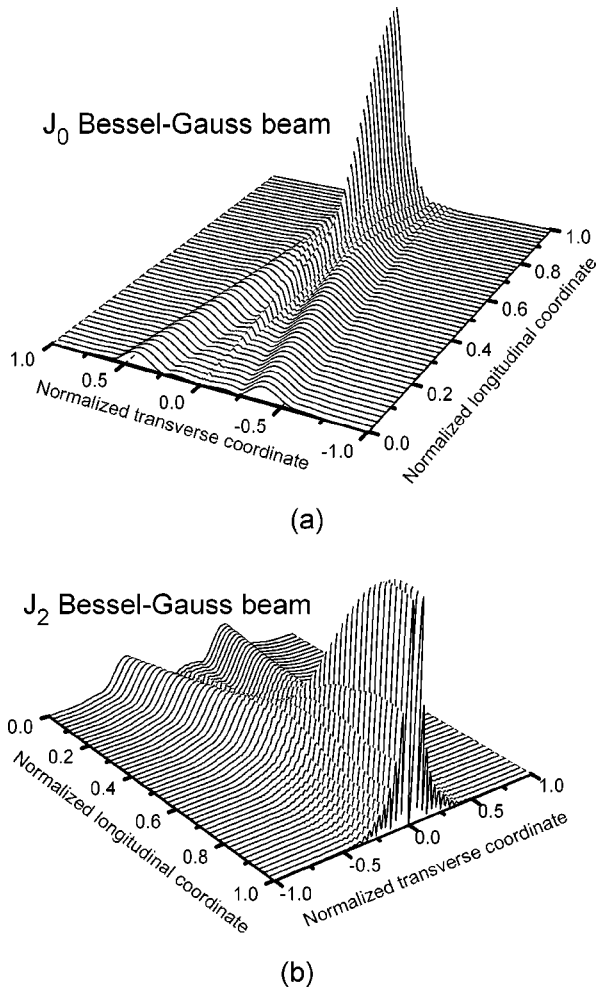

Fig. 8. Passive three-dimensional intracavity field distributions in the resonator with spherical output mirror ($R = 10\,L$): (a) dominant J_0 Bessel–Gauss beam, (b) second-order J_2 Bessel–Gauss beam.

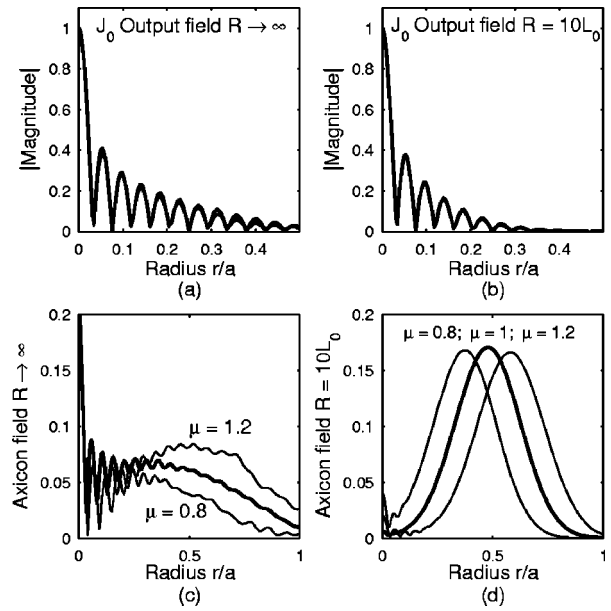

Fig. 9. Transverse field pattern at the output and axicon planes corresponding to the length factors $\mu = 0.8$, 1, and 1.2 for both plane and spherical output mirrors.

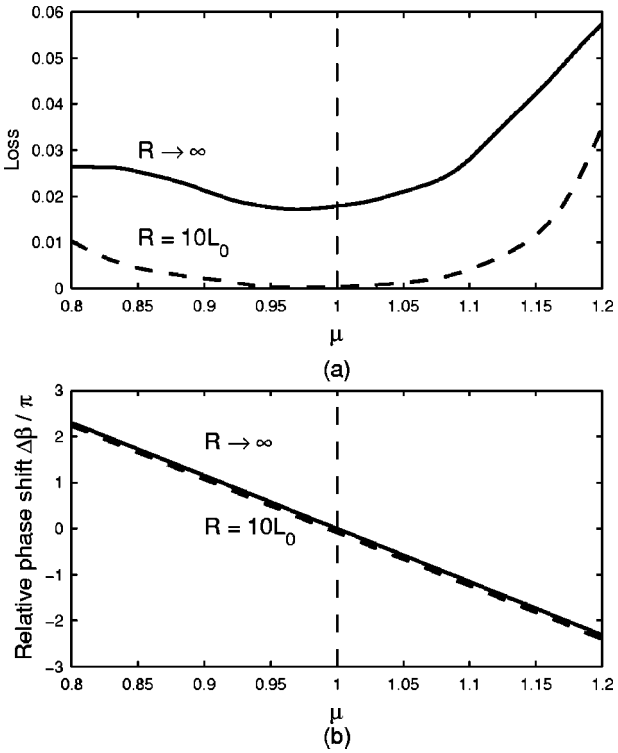

Fig. 10. Loss and resonant frequency shift behavior as a function of length factor μ for both plane and spherical output mirrors.

to study the effect of varying the cavity length while maintaining fixed the axicon parameters. The relevant output characteristics are the transverse field profile, the diffractive loss, and the resonant frequency shift. We first define the length factor $\mu = L/L_0$, where L_0 is the unchanged cavity length in Eq. (3) and now L is the current length.

The output fields of the zero-order mode for $\mu = \{0.8, 1, 1.2\}$ are shown in Figs. 9(a) and 9(b) for plane and spherical output mirrors, respectively. Note that the curves coincide almost completely; this means that the spatial frequency k_t remains constant under a change of μ. This fact occurs because each constituent plane wave within the cavity is forced by the axicon to propagate with the same characteristic angle θ_0, independently of the cavity length. The only major difference between the curves plotted in Figs. 9(a) and 9(b) is that the curves for $\mu = 0.8$ and 1.2 decrease slightly faster than the curve for $\mu = 1$, mainly as a result of the different loss characteristics. As illustrated in Figs. 9(c) and 9(d), the transverse field at the axicon (and consequently the intracavity field distribution) is found to move radially out with increasing μ, as expected from the fact that intracavity intensity tends to locate around the geometric cone predicted in Section 3.

The loss and frequency shift behavior as a function of the length factor μ is depicted in Fig. 10 for both plane and spherical output mirrors. A notable characteristic of each loss curve is that the minimum occurs not at $\mu = 1$ but approximately at $\mu \sim 0.97$; this fact is a result of the wave nature of the fields and cannot be predicted with geometrical optics. As expected, loss decreases as the radius of curvature decreases because the concavity tends to concentrate the field around the optical axis.

For the case of varying the cavity length, we redefine the relative phase shift as $\Delta\beta = \beta(L) - \beta_{L_0}$, where $\beta(L)$ is the phase of the eigenvalue as a function of the length L and β_{L_0} corresponds to the unchanged case when $L = L_0$. Changing the length leads to a variation of the resonant frequency according to Eq. (17). The resonant frequency is found to decrease with increasing length factor, as shown in Fig. 10(b), where we can note that the behavior is practically linear.

The results depicted in Figs. 9 and 10 were determined by solving the eigenequation (15) for a range of μ. To corroborate these curves, we also have applied the Fox and Li algorithm to find the resonant properties of the dominant field for different length factors, and an excellent agreement was obtained between both approaches.

6. PROPAGATION OF THE OUTPUT BEAM

In Figs. 11(a) and 11(b), we have simulated the evolution of the J_0 Bessel–Gauss beam along the plane x–z from the output coupler to a distance $1.2L$ ahead for plane and concave ($R = 10L$) output mirrors, respectively. We have applied a two-dimensional beam propagation method based on a fast Fourier transform, taking as initial conditions the radial distributions shown in Figs. 4(c) and 5(c). According to the geometrical prediction depicted in Fig. 1(c), the maximum propagation distance is L. Since Bessel–Gauss beams have a set of circular rings, one can see easily the conical region where the beam preserves invariance. It can also be seen in Fig. 11(b) that the concavity of the output coupler smooths the oscillations of the axial intensity that are present for the flat mirror case. This further demonstrates the high modal discrimination of the ABGR with spherical mirror and shows that the beam reaches a stable fundamental

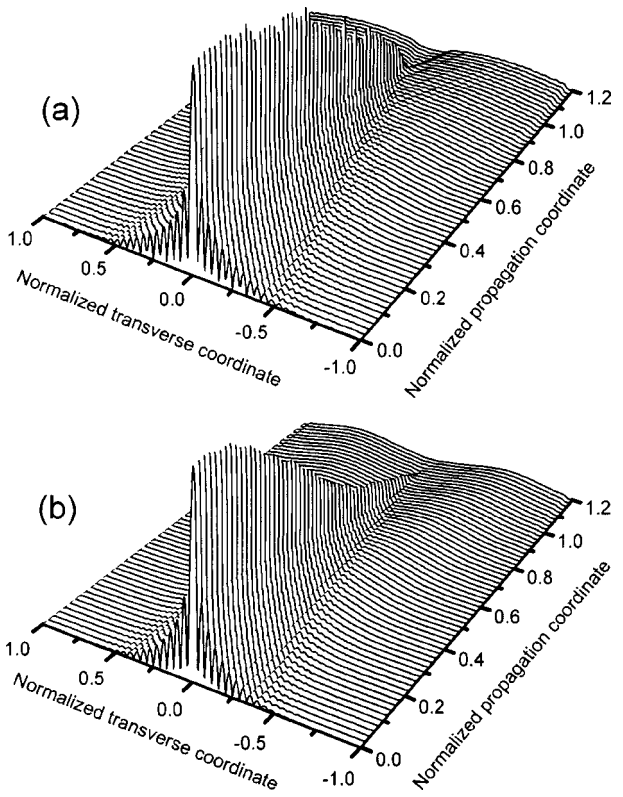

Fig. 11. Numerical propagation of the output beam of the ABGR for (a) plane and (b) spherical $R = 10L$ output couplers.

mode having a Bessel–Gauss shape. Beyond the invariance region the beam takes a ring transverse shape that expands out as the field propagates.

For most applications the focusing properties of the output beam are of crucial importance. For Bessel–Gauss beams it is well known that the image in the focal plane corresponds to a circular ring. The three-dimensional spatial evolution of focused IOFs with arbitrary intensity distribution is analyzed in detail in Ref. 27. The beam quality factor M^2 has not been evaluated here.[28] However, the field profile and the evolution plots presented here are much more significant in showing the Bessel–Gauss form of the beam, which is the main goal of this paper.

7. CONCLUSIONS

A detailed analysis of the resonating modes in the axicon-based Bessel–Gauss resonator with spherical output mirror has been presented. Formulas of the radial spatial frequency and the Gaussian width of the output field have been given explicitly in terms of the axicon parameters, the cavity length, and the spherical output coupler. The paraxial ray analysis provides a useful geometric framework to find the self-consistency condition of stable trajectories within the cavity. This analysis revealed the existence of self-reproducing modes after two round trips, independently of the radius of curvature of the output mirror. We also gave the geometric conditions necessary to have stable trajectories after one and two round trips. To do this, we have proposed a new inhomogeneous *ABCD* matrix for the axicon. Our *ABCD* matrix formalism could be applied to other geometric analysis involving the propagation of rays through axicons in the paraxial regime.

We have shown the usefulness of the eigenvalue matrix method based on the Huygens–Fresnel integral for performing numerical calculations of the Bessel–Gauss modes. In particular, the advantage of using this method is that it offers a fast procedure to find the eigenfields and the eigenvectors (i.e., losses and frequency shifts) of the resonating modes at the output coupler and the axicon plane. In addition, a fast-Fourier-transform-based Fox and Li method has been implemented to (a) describe the three-dimensional intracavity field distribution, (b) corroborate our geometrical predictions, and (c) confirm the results obtained with the Huygens–Fresnel integral method. Excellent agreement between both approaches was obtained.

The effects of varying the radius of curvature of the output mirror and the cavity length on the behavior of the Bessel–Gauss modes have been studied as well. Our analysis revealed that the radial spatial frequency is completely defined by the axicon parameters and is independent of the cavity length. The curvature radius of the output coupler can be adjusted to tune the width of the Gaussian modulation of the Bessel–Gauss field. We have found that the diffractive loss is minimized when cavity length is approximately 97% of the value predicted by geometrical optics. The analysis presented in this paper can be extended to unstable resonators by changing the concave spherical mirror into a convex spherical mirror.

ACKNOWLEDGMENTS

The authors acknowledge financial support from CONACYT-México under grant I-36456 and from the Tecnológico de Monterrey Research Chair in Optics under grant CAT-007.

Julio C. Gutiérrez-Vega can be reached by e-mail at juliocesar@itesm.mx.

REFERENCES

1. J. Durnin, "Exact solutions for nondiffracting beams. I. The scalar theory," J. Opt. Soc. Am. A **4**, 651–654 (1987).
2. J. Durnin, J. J. Micely, Jr., and J. H. Eberly, "Diffraction-free beams," Phys. Rev. Lett. **58**, 1499–1501 (1987).
3. F. Gori, G. Guattari, and C. Padovani, "Bessel–Gauss beams," Opt. Commun. **64**, 491–495 (1987).
4. E. Abramochkin and V. Volostnikov, "Spiral-type beams," Opt. Commun. **102**, 336–350 (1993).
5. S. Chávez-Cerda, G. S. McDonald, and G. H. C. New, "Nondiffracting beams: travelling, standing, rotating and spiral waves," Opt. Commun. **123**, 225–233 (1996).
6. C. Paterson and R. Smith, "Helicon waves: propagation-invariant waves in a rotating coordinate system," Opt. Commun. **124**, 131–140 (1996).
7. R. Piestun and J. Shamir, "Generalized propagation-invariant wave fields," J. Opt. Soc. Am. A **15**, 3039–3044 (1998).
8. J. C. Gutiérrez-Vega, M. D. Iturbe-Castillo, and S. Chávez-Cerda, "Alternative formulation for invariant optical fields: Mathieu beams," Opt. Lett. **25**, 1493–1495 (2000).
9. J. H. McLeod, "The axicon: a new type of optical element," J. Opt. Soc. Am. **44**, 592–597 (1954).
10. G. Indebetouw, "Nondiffracting optical fields: some remarks on their analysis and synthesis," J. Opt. Soc. Am. A **6**, 150–152 (1989).

11. G. Scott and N. McArdle, "Efficient generation of nearly diffraction-free beams using an axicon," Opt. Eng. **31**, 2640–2643 (1992).
12. J. Turunen, A. Vasara, and A. T. Friberg, "Holographic generation of diffraction-free beams," Appl. Opt. **27**, 3959–3962 (1988).
13. A. Vasara, J. Turunen, and A. T. Friberg, "Realization of general nondiffracting beams with computer-generated holograms," J. Opt. Soc. Am. A **6**, 1748–1754 (1989).
14. Wen-Xiang Cong, Nan-Xian Chen, and Ben-Yuan Gu, "Generation of nondiffracting beams by diffractive phase elements," J. Opt. Soc. Am. A **15**, 2362–2364 (1998).
15. J. Durnin and J. H. Eberly, "Diffraction free arrangement," U.S. patent 4,887,885, December 19, 1989.
16. K. Uehara and H. Kikuchi, "Generation of nearly diffraction-free laser beams," Appl. Phys. B **48**, 125–129 (1989).
17. P. Pääkkönen and J. Turunen, "Resonators with Bessel–Gauss modes," Opt. Commun. **156**, 359–366 (1998).
18. P. A. Bélanger and C. Paré, "Optical resonators using graded-phase mirrors," Opt. Lett. **16**, 1057–1059 (1991).
19. P. A. Bélanger, R. L. Lachance, and C. Paré, "Super-Gaussian output from a CO_2 laser by using a graded-phase mirror resonator," Opt. Lett. **17**, 739–741 (1992).
20. J. Rogel-Salazar, G. H. C. New, and S. Chávez-Cerda, "Bessel–Gauss beam optical resonator," Opt. Commun. **190**, 117–122 (2001).
21. J. Rogel-Salazar, G. H. C. New, P. Muys, J. C. Gutiérrez-Vega, and S. Chávez-Cerda, "Bessel–Gauss resonators," in *Laser Resonators IV*, A. V. Kudryashov and A. H. Paxton, eds., Proc. SPIE **4270**, 52–63 (2001).
22. A. N. Khilo, E. G. Katranji, and A. A. Ryzhevich, "Axicon-based Bessel resonator: analytical description and experiment," J. Opt. Soc. Am. A **18**, 1986–1992 (2001).
23. H. Kogelnik and T. Li, "Laser beams and resonators," Proc. IEEE **54**, 1312–1329 (1966).
24. A. E. Siegman, *Lasers* (University Science, Mill Valley, Calif., 1986).
25. W. H. Press, B. P. Flannery, S. A. Teukolsky, and W. T. Vetterling, *Numerical Recipes* (Cambridge U. Press, Cambridge, UK, 1986), Chap. 11.
26. W. P. Latham, Jr., and G. C. Dente, "Matrix methods for bare resonator eigenvalue analysis," Appl. Opt. **19**, 1618–1621 (1980).
27. S. Chávez-Cerda and G. H. C. New, "Evolution of focused Hankel waves and Bessel beams," Opt. Commun. **181**, 369–378 (2000).
28. R. Borghi and M. Santarsiero, "M^2 factor of Bessel–Gauss beams," Opt. Lett. **22**, 262–264 (1997).